ON THE ORIGIN OF SELF-ORGANIZATION OF SiO$_2$ NANODOTS DEPOSITED BY CVD ENHANCED BY ATMOSPHERIC PRESSURE REMOTE MICROPLASMA

G. Arnoult[1], T. Belmonte[1],[*], F. Kosior[1], M. Dossot[2], G. Henrion[1]

[1]Institut Jean Lamour, Department of Physics and Chemistry of Solids and Surfaces, UMR 7198 CNRS, Nancy-Université, Parc de Saurupt, CS 14234, F-54042 Nancy Cedex, France

[2] Laboratoire de Chimie Physique et Microbiologie pour l'Environnement, UMR 7564 CNRS - Université Henri Poincaré, Nancy-Université, 405, rue de Vandoeuvre, F-54600 Villers-lès-Nancy

[*] Corresponding author. Fax: +33.3.83.53.47.64

E–mail: thierry.belmonte@mines.inpl-nancy.fr

ABSTRACT

The origin of organization of nanostructured silica coatings deposited on stainless steel substrates by remote microplasma at atmospheric pressure is investigated. We show by resorting to thermal camera measurements coupled with modelling that deposition, limited to a few seconds in time, occurs at low temperature (~below 420 K) although the gas temperature may reach 1400 K. Raman analyses of deposited films with thicknesses below 1 µm show the presence of oxidized silicon bonded to the metallic surface. The origin of nanodots is explained as follows. Close to the microplasma nozzle, the concentration of oxidizing species and/or the temperature being high enough, a silica thin film is obtained, leading to ceramic-metallic oxide interface that leads to a Volmer-Weber growth mode and to the synthesis of 3D structures over long treatment times. Far from the nozzle, the reactivity decreasing, thin films get a plasma-polymer like behaviour which leads to a Franck-Van der Merwe growth mode and films with a higher density. Other nanostructures, made of hexagonal cells, are observed but remain unexplained.

1. INTRODUCTION

Many research groups are involved in plasma assisted nanofabrication which is an emerging field for the production of various nanostructured materials, nanostructures and elements of nanodevices [1-10].

Self-organization and patterning of surfaces have been attempted in many ways recently [11-18]. For instance, excimer laser irradiation at ambient temperature has been employed successfully to produce nanostructured silicon surfaces [11]. Self-assembly may occur spontaneously but may also be driven by various means like physical, chemical or biological templates, or induced by fields like pressure gradient, electric field, magnetic field, light, laser, etc. [12-14]

The need for a better understanding of fundamental physical phenomena governing the synthesis of nanostructures on surfaces submitted to plasmas has recently motivated basic researches [19-22]. These latter works could provide clear explanations of underlying phenomena governing the growth of organized nanostructures on surfaces.

In a recent work [10], we showed how to get self-organized SiO_2 nanodots by chemical vapor deposition out of hexamethyldisiloxane (HMDSO) and atmospheric pressure remote Ar–O_2 microwave plasma operating at high temperature (1200–1600 K). The needle-like afterglow is laminar and is less then 1 mm in diameter. [23]

When the film being deposited is thin enough (< 500 nm), nanodots of silica with a mean diameter close to 500 nm get interconnected to create threads (Fig. 1a). The structure can grow in three dimensions when the deposition time increases (Fig. 1b). When the coating becomes thicker (~1 µm), and for relatively high contents in HMDSO, SiO_2 walls forming hexagonal cells are obtained on a SiO_2 sublayer (Fig. 1c). For even thicker coatings (> 1 µm), droplet-shaped coatings with a Gaussian distribution in thickness over their width are deposited. When the coatings are put under primary vacuum, the structure breaks into pieces,

creating "nestlike structures" made of nanoribbons (Fig. 1d). We showed that these nanostructures required to be deposited close enough (~ 4 mm) to the nozzle of the cavity through which the remote plasma exits [10]. Far from it (> 10 mm), homogeneous films are deposited.

Several phenomena could be responsible for the formation of these nanostructures. Similar patterns are obtained by surface dewetting at high temperature [24, 25] where advanced models are now available in some cases (drying liquid film) to describe phenomena. Other works [26, 27], dealing with buckling of thin films exhibit patterns that are vey close to those described herein.

In this work, we wish to clarify the mechanisms responsible for the synthesis of these nanostructures. The sketch of this work is as follows: after a description of the experimental set-up, we shall describe the model of heat transfer used to determine the temperature reached by the topmost surface of the sample. Next, we shall present surface analyses by X-Ray Diffraction (XRD), Secondary Ion Mass Spectrometry (SIMS) and Raman spectroscopy. Finally, we shall discuss the results to discriminate among the various possible growth mechanisms.

2. EXPERIMENTAL SET-UP

The experimental set-up is shown in Fig. 2. A detailed description is provided elsewhere [10]. Briefly, the atmospheric microwave plasma is created in a fused silica tube located in a 2.45 GHz resonant cavity. The power supply delivers 70 W under the present conditions. The plasma (Ar–9.1 vol.%O_2) is centered on the tube axis by a fan and neutral species exit the copper cavity through a tiny hole (400 µm in diameter). We used a total gas flow rate of 275 sccm. Under these conditions, a straight beam containing oxygen atoms and other neutral excited species of oxygen is produced. The remote microplasma is mixed with an argon–

hexamethyldisiloxane (HMDSO – $(CH_3)_3$-Si-O-Si-$(CH_3)_3$) mixture (Fig. 2). This mixture is introduced through a slit (h=1 mm $\times$ w=10 mm) and obtained as follows: an argon flow with a sufficiently low flow rate (hereafter written $y < 30$ sccm) is used so as to consider it fully extracts the vapor pressure of the liquid HMDSO that is regulated in temperature by a thermostat at 298 K. Then, the HMDSO flow rate is 0.055y sccm. We introduce downstream an additional flow of argon (200 sccm) to set the dilution of the precursor. The treatment starts when the sample is located in front of the beam, the Ar–HMDSO mixture flowing.

Samples used are stainless steel disks (1 mm in diameter and 10 mm in diameter). Steel was used because of its passive layer which is not significantly affected when temperature rises. They are polished mechanically (final stage 1 µm diamond paste) and ultrasonically cleaned in ethanol before treatment.

Raman spectra are collected with a T64000 Raman spectrometer by Jobin-Yvon used in confocal and backscattering microscopy mode. The wavelength of the incident light produced by an argon laser is 514.5 nm. The irradiance of the sample is 50 kW cm^{-2}. The magnification given by the objective lens is $\times$100 and the numerical aperture is 0.85. The CCD detector is cooled at 140 K by liquid nitrogen to enhance its sensibility and to decrease the background noise. Although the T64000 spectrometer is a dispersive system made of three monochromators, analyses are performed in "direct" mode where only one grating (1800 grooves per millimetre) is used. Under these conditions, Rayleigh and Raman diffusions have to be separated by an appropriate filter. We used an Edge filter at 514 nm operating down to 100 cm^{-1}. The main advantage of this mode is to get a high brightness of the CCD with regards to a mode using a pre-monochromator stage with two gratings. The slit width, set at 100 µm, gives a resolution of 3 cm^{-1}. Each presented spectrum is a mean value of 5 spectra acquired for duration between 30 and 120 s depending on the location: the acquisition time

increases when we move along the radius from the center outward, the thickness of the deposit decreasing.

Infra-red measurements are performed with a FLIR SC7200-MB camera with a time step of 5.6 µs. Experimental conditions retained are: H=2.8 or 6.0 mm. y=21 sccm (2420 ppm). Substrate emissivity was calibrated by using a heating device between 300 K and 800 K. The following law was derived for the stainless steel used:

$$\varepsilon(T) = -2.15549 \times exp\left(-\frac{T}{139.5691}\right) + 0.31349$$

(1)

It corresponds to usual values encountered for emissivity of polished stainless steels in this range of temperature.

3. MODELLING

One of the key values to know accurately for this work is the surface temperature of the stack made by the substrate and its coating. A direct access to this temperature is not possible. Indeed, the heated side of the substrate, which behaves as a mirror, reflects the light emitted by the heated wall of the plasma cavity through which the remote plasma exits. This wall is much hotter than the substrate. Indeed, when the experiment begins, the substrate is put under the flame and its temperature is 300 K. On the contrary, the plasma is at steady state and the microwave cavity in thermal equilibrium with it. Then, experimental measurements of the temperature are performed on the back side of the substrate. The surface temperature of deposited silica is determined by solving the heat equation in the stack (Fig. 3):

$$\frac{\partial \rho C_p T}{\partial t} + \nabla.\left(-\lambda \vec{\nabla} T\right) = 0$$

(2)

where is ρ the material density, C_p its specific heat and λ its thermal conductivity. Solution is calculated in transient and in 2D. Boundary conditions are determined from correlations. NO interface resistance was assumed between the substrate and the coating.

Wall 1. This problem was treated by Remie *et al.* [28]. These authors studied the case of an impinging laminar flame jet to a flat plate. In our case, which is identical, the plasma corresponds to the flame, the cavity wall to the burner and the afterglow to the free jet region. The heat flux heated by a plasma at T_∞ located at a distance greater than the diameter δ of the afterglow is given by:

$$q = h_1(T_s - T_\infty) \quad 0 < 2r/\delta < 1$$

$$q = h_1(T_s - T_\infty)\exp(-0.45(2r/\delta - 1)) \quad 2r/\delta \geq 1 \tag{3}$$

where q is the heat flux, h_1 the heat transfer coefficient at wall 1, T_s, the substrate temperature, r the radius. Then, h_1 is given by the following correlation:

$$h_1 = \frac{\lambda_a}{H}\sqrt{\frac{UH}{\alpha}}\exp\left(-0.28\,Pr^{0.4}\right) \tag{4}$$

Here, λ_a is the thermal conductivity of the afterglow, H cavity wall-to-plate distance, U the uniform flow velocity, α the afterglow thermal diffusivity and Pr, the Prandtl number calculated for the afterglow:

$$Pr = \frac{\mu_a C_{p,a}}{\lambda_a} \tag{5}$$

where μ_a is the afterglow dynamic viscosity and $C_{p,a}$ its specific heat. The gas properties used to determine h_1 are given in Table 1 and are calculated at $T_f = (T_s + T_\infty)/2$.

The presence of a thin silica layer was included in the calculation. The deposition rate being very high for a CVD process ($\sim$1500 µm h^{-1}), we chose to take it into account. The thickness profile of this layer along the radius r, regardless of its structure, may be described as a function of time by the following empirical relation:

$$\eta(r,t) = \left(\frac{A_1(t)}{w_1\sqrt{\frac{\pi}{2}}}\right)\exp\left(-2\left(\frac{r}{w_1}\right)^2\right) + \left(\frac{A_2 A_1(t)}{w_1\sqrt{\frac{\pi}{2}}}\right)\exp\left(-2\left(\frac{r}{w_2}\right)^2\right) \tag{6}$$

where w_1, w_2 and A_2 are constants and A_1, an affine function of time. In the experimental conditions retained experimentally for comparison with modelling results, we have: $w_1=1.22894$; $w_2=3.74288$; $A_2=1.22082$; $A_1 (t)=0.316124 \times t$ (s) and r expressed in mm.

Wall 2. We used the following correlation:

$$\overline{Nu}_L = 0.68 + \frac{0.67 Ra^{0.25}}{\left(1 + \left(\frac{0.492}{Pr}\right)^{9/16}\right)^{4/9}} \tag{7}$$

describing heat transfer in the case of a vertical wall cooled by laminar and turbulent free convection when the Rayleigh number,

$$Ra = \frac{\rho_a^2 g \beta_a C_{p,a}}{\lambda_a \mu_a} (T_{room} - T_s) L^3 \tag{8}$$

is in the range [0 - 10^9] [29]. Here, T_{room} is the room temperature, β_a is the afterglow compressibility factor and g, the gravitational constant. L is the characteristic dimension of the surface, *i.e.* the sample thickness.

The heat transfer coefficient is determined readily by the relation:

$$h_2 = \frac{\overline{Nu}_L L}{\lambda_a} \tag{9}$$

Wall 3. The issue of the heat transfer by natural convection from a downward-facing round plate was treated by [30] for a disk of diameter $D=2R$:

$$\overline{Nu}_D = 1.759 Ra^{0.13} \text{ if } 3 \times 10^2 < Ra < 10^4$$

$$\overline{Nu}_D = 0.9724 Ra^{0.194} \text{ if } 10^4 < Ra < 3 \times 10^7 \tag{10}$$

where

$$Ra = \frac{\rho_a^2 g \beta_a C_{p,a}}{\lambda_a \mu_a} (T_{room} - T_s) D^3 \tag{11}$$

and finally:

$$h_3 = \frac{\overline{Nu_D} D}{\lambda_a}$$

(12)

Mesh. We used a triangular mesh consisting of 241,388 elements. It has been refined around the SiO$_2$ boundary with a size of elements of 0.2 µm maximum. Boundaries where the flow is outgoing, have a maximum element size of 0.5 µm, which finally gives us 2,547,121 degrees of freedom. Time steps are taken equal to 0.1 s during the first 3 seconds and to 1 s from 3 to 10 s. Solution was obtained by using the COMSOL MULTIPHYSICS® software coupled with MATLAB® [31]. This type of triangular mesh is best suited to using the software COMSOL MULTIPHYSICS® contrary to the rectangular mesh.

Data. Gas phase properties were determined from data reported in Table 1 using mixing classical laws available in [32] for instance. Solid properties are reported in Table 2. We assumed that the substrate temperature remains low enough to avoid phase transformation (in the case of copper whose melting temperature is 1357.77 K).

4. RESULTS AND DISCUSSION

Nanostructures require to be deposited close enough (~ 3-4 mm) to the nozzle of the cavity through which the remote plasma exits. Otherwise, homogeneous films are deposited. If these homogeneous films, when thin enough, are post-treated at 4 mm from the nozzle, *i.e.* located in the Ar-O$_2$ remote plasma without any HMDSO flux, their structure evolves to give the same nanodots of silica observed for appropriate conditions. The role played by stress, by the temperature or by surface reactivity has to be clarified.

4.1. Surface temperature

Experimental data giving the evolution in time and position of the temperature distribution of the backside surface of the substrate, when a silica coating is deposited or not, are depicted in Fig. 4a for a point located at $r = 0$ and in Fig. 4b along a line going from $r = 0$ to r = 5 mm. Two situations are studied: the afterglow temperature is 1200 K (*i.e.* Ar-20vol.%O$_2$ plasma

9

mixture) and H=6.0 mm or it is 1400 K (*i.e.* Ar-9.1vol.%O_2 plasma mixture) and H=2.8 mm. Contrary to copper, which was also used in unreported experiments, the passive oxide layer of stainless steel is not significantly modified by a 30-second treatment, unaffecting the emissivity.

The experimental results could be nicely reproduced by the model in the two studied conditions by changing h_2 and h_3 in Eqs. (9) and (12) by a factor of 1.65 for H=6.0 mm and 2.35 for H=2.8 mm, what is quite convincing. Indeed, heat transfer coefficients are given only within a factor of two [33] and determined in steady state conditions. At low temperatures, the discrepancy is more important, probably because of validity limit of correlations used in the model when the system is far from steady state.

From these results, we can predict the highest temperature reached by the surface directly submitted to the afterglow (Fig. 5). Clearly, when $H = 2.8$ mm, we observe that during the first three seconds, the temperature does not rise above 420 K, clearly demonstrating that the origin of the nanostructure is not associated with a high surface temperature, like in the case of thin film dewetting [24]. A maximum variation of the temperature of +3 K is measured when the coating grows on the substrate with regards to an uncoated surface. The deposition of a thermal barrier does affect the temperature of the topmost surface by increasing it, as expected, but the weak thickness of the growing layer and the low temperature range reached during the experiment makes this temperature rise totally negligible.

4.2. Surface analyses

Deposited thin films were analyzed at their center by SIMS (Fig. 6). We notice that the carbon content in the layer may be considered as negligible when deposition occurs close to the nozzle (H=3 mm). The [O]/[Si] ratio in the layer is constant. We also observe a kind of

diffusion profile in the steel for silicon and oxygen. It is due to the presence of these species in the oxidized steel. XRD analyses show that the silica layer is amorphous.

Raman Spectroscopy was used to characterize the nature of the deposit versus the distance r from its center. Raman peaks of silica are determined by comparison with an untreated stainless steel substrate (Fig. 7). Peaks at 488, 690, 755, 796, 960 and 1048 cm^{-1} are identified as specific to silica.

Generally, a broad band around 440 cm^{-1} appearing in silica spectra is assigned either to a symmetric bending vibration of the Si–O–Si linkage with oxygen motion perpendicular to the Si–Si line or to the O–Si–O deformation of the coupled "tetrahedra" SiO$_4$ groups. The large FWHM is attributed to the wide distribution of the intertetrahedral Si–O–Si angles within the structure. Frequency shifts and band narrowing to higher energies of this band with increasing temperature [34, 35] have been attributed to a decrease of the average intertetrahedral angles.

If the band near 800 cm^{-1} is made of two overlapping relatively narrow bands, it can be associated with motions of Si against its tetrahedral cage of oxygen atoms [36]. The energies correspond to Si–O stretching vibrations. The band shifts to lower frequencies with increasing temperature [35].

The peak at a wavenumber of 960 cm^{-1} may rather be assigned to Si–O vibration in a non-stoichiometric silica [37] than to non-bridging oxygen atoms, also known as NBO groups [38]. Indeed, these latter groups mainly appear for silicate glasses modified by the incorporation of alkali or/and alkali-earth elements.

The band centered at 1050 cm^{-1} may correspond to asymmetric stretching vibrations associated with two different populations of Si–O–Si angles which constitute different domains within the glass [39]. These bands may also arise from TO-LO splitting on a noncentrosymmetric vibration by the long-range Coulomb field [40]

11

D1 and D2 bands of silica usually appear around 493 and 606 cm^{-1} [41]. These sharp defect bands are totally polarized with full width at half maximums much narrower than those of the regular network bands. These bands have been associated to breathing vibrations of oxygen atoms in four- and three-membered rings, respectively [42, 43]. D2 band is clearly absent from the present spectrum and D1 band is not visible.

The Raman spectra of the deposited silica present features that are quite close to those of a high temperature silica.

Peaks at 690 and 755 cm^{-1}, denoted by a star in Figs. 7 and 8, are to be identified. These peaks are not commonly found in silica-like materials. We notice that the intensities of these two lines increases from the center outward, whereas other lines decreases (Fig. 9). Since the thickness of the layer decreases, these Raman peaks being characteristic of the silica coating, we suggest to assign them to bonds with elements from the substrate. According to reference [44], the band at 690 cm^{-1} may be associated with the Si–O–Fe(Co) vibration. In this study, the effect of the annealing temperature upon the synthesized nanocomposite $CoFe_2O_4$–SiO_2 samples was investigated. It was verified that, when the annealing temperature increases (>800 K), a low-intensity Raman peak around 690 cm^{-1} appears. On the other hand, Calistru *et al.* [45] observed Raman peaks at 690 and 764 cm^{-1} that are detected in Cr_4^+:Mg_2SiO_4 and not in Mg_2SiO_4. Therefore, we suggest that Si-O-(Fe,Cr) bonds are created between the deposited material and the oxidized surface of the stainless steel. Indeed, oxidation of such an alloy leads to the growth of mixed iron-chromium oxide [46].

Now, if we observe the behaviour of the peak at 488 cm^{-1} (Fig. 10), we notice that the peak becomes broader from the centre to the edge of the coating. When the thickness increases, the Raman peak is shifted by about 13 cm^{-1}, showing a high level of stress at the edge. Then, the silica layer is submitted to a radial gradient of stress that tends to wrinkle the film perpendicularly to the radius.

4.3. Discussion

Scratches present on the surface are created by mechanical polishing. They are favoured sites to enhance nucleation. The size of these defects plays an important role. Indeed, when the stainless steel is prepared by polishing with a 1 µm diamond paste, the mean width of the scratches is close to this value. It is also the thickness at which we have a transition from dots directly deposited on the surface (Fig. 1a) to cells appearing on a silica sub-layer (Fig. 1c). In Fig. 1a, we see that the mean distance between two adjacent rows of dots is close to 1 µm. The growth of dots rather than a continuous film is certainly due to the surface energy of the passive layer of the steel surface that favours a Volmer-Weber growth mode rather a Franck-Van der Merwe growth mode when silica is deposited. Hemispherical nuclei are synthesised and bonded to the passive layer by means of Si-O-(Fe,Cr) bonds that are created between the deposited material and the oxidized surface. When the coarsening of these nanostructures occurs, *i.e.* close to 1 µm in thickness, active species from the gas phase are in contact with a continuous silica film and no longer with the passive layer.

Since this conclusion cannot be drawn if the distance between the nozzle and the substrate is too big, we may assume that the same kind of surface bonding cannot be achieved. This could be due to the introduction of carbon in the layer, due to a slower dissociation of the HMDSO precursor in the remote plasma. This could either result from a lower concentration of active species in the gas phase that get depleted during their transport or from the drop of the remote plasma temperature.

To check this assumption, we performed SIMS measurement along a diameter on the coatings deposited at different distances to determine the evolution of the carbon content. Results are depicted in Fig. 11. While no carbon is found close to the nozzle, we measure increasing carbon amounts in the films beyond 6 mm. From 6 to 13 mm, the [C]/[Si] ratio increases at the center of the deposit by one order of magnitude, giving to coatings a polymer-like

behavior rather than ceramic-like behavior. Consequently, we assign the origin of the nanostructure the lack of carbon in the film.

The inorganic behavior of silica reduces the accommodation possibility of the deposit on steel. On the contrary, the presence of carbon leads to a polymer-like deposit where stress is more easily relaxed. Carbon may directly affect the growth mode and likely control the level of stress, acting like a control element of the deposit structure if its concentration is monitored.

The development of stress as shown by Raman analyses is likely responsible for the growth of hexagonal cells appearing on a silica sublayer. It may be also associated with a change in the carbon composition from the coating-substrate interface to the topmost surface of the coating but this point has not been investigated yet. In Fig. 1c, we determine four main directions, two by two perpendicular, along which the cell walls grow. Two of them are clearly associated with the shape of the coating: along concentric circles and along their radius. The two other directions are obviously not associated with scratches due to polishing because the mean distance between them is much higher than 1 µm (~25 µm). For the moment, no clear explanation can be provided to explain the origin of this specific structure.

5. Conclusion

In this work, we could demonstrate that:

- Surface temperature is limited to a few tens of Kelvin above room temperature, enabling us to discard dewetting as a possible process for surface nanostructuration

- Raman analyses showed the presence of bonds between the coating and the native oxide of the stainless steel. The development of stress when the coating thickens was also evidenced.

14

- SIMS analyses proved than carbon is incorporated in the coating when the distance between the nozzle and the substrate increases.

We assigned the origin of the nanostructure to the lack of carbon in the film. The presence of scratches on the surface of the substrate due to mechanical polishing intervenes to partly orientate the growth. However, when hexagonal cells are obtained, their influence is negligible and no clear explanation is yet available to describe to growth of these patterns.

Further analyses are on the way to clarify the mechanism responsible for the formation of hexagonal cells. Titanium Tetra-Iso-Propoxide will promptly be used instead of HMDSO to check the validity of the model proposed herein but in another system.

REFERENCES

[1] Cheng Q J Xu S Long J and Ostrikov K 2007 Appl. Phys. Lett. **90** 173112

[2] Ostrikov K 2005 Rev. Mod. Phys. **77** 489

[3] Sankaran R M Holunga D Flagan R C and Giapis K P 2005 Nano Lett. **5** 537

[4] Yuan L Zhong X and Ostrikov K 2008 Nanotechnology **19** 155304

[5] Cvelbar U Ostrikov K and Mozetič M 2008 Nanotechnology **19** 405605

[6] Shimizu Y Sasaki T Ito T Terashima K and Koshizaki N 2003 J. Phys. D: Appl. Phys. **36** 2940

[7] Mariotti D Chandra Bose A and Ostrikov K 2009 IEEE Trans Plasma Sci **37** 1027

[8] Nozaki T and Okazaki K 2006 Pure Appl. Chem. **78** 1157

[9] Meguro T Tsuji N Saito S Yamamoto Y Mise T and Watanabe K 2008 Surf. Coat. Technol. **202** 5356

[10] Arnoult G Belmonte T and Henrion G 2010 Appl. Phys. Lett. **96** 101505

[11] Kumar P Ghanashyam Krishna M and Bhattacharya A K 2009 J. Nanosci. Nanotechnol. **9** 3224

[12] Kumar P 2010 Micro and Nano Letters **5** 110

[13] Kumar P 2010 Nanoscale Research Letters **5** 1367

[14] Prokopenko M 2008 Advances in Applied Self-organizing Systems, Advanced Information and Knowledge Processing Part I, 3-17

[15] Frost F Fechner R Ziberi Völlner J Flamm D and Schindler A 2009 J. Phys.: Condens. Matter **21** 224026

[16] Bennewitz R 2006 J. Phys.: Condens. Matter **18** R417

[17] Kerner B S and Osipov V V 1990 Sov. Phys. Usp. **33** 679

[18] Brune H Giovannini M Bromann K and Kern K 1998 Nature **394** 451

[19] Chen Z Cvelbar U Mozetič M He J and Sunkara M K 2008 Chem. Mater. **20** 3224

[20] Levchenko I Ostrikov K Mariotti D and Švrček V 2009 Carbon **47** 2379

[21] Levchenko I Ostrikov K and Mariotti D 2009 Carbon **47** 313

[22] Ho J C Levchenko I and Ostrikov K 2007 J. Appl. Phys. **101** 094309

[23] Arnoult G Cardoso R P Belmonte T and Henrion G 2008 Appl. Phys. Lett. **93** 191507

[24] Xie R Karim A Douglas J F Han C C and Weiss R A 1998 Phys. Rev. Lett. **81** 1251

[25] Schwartz L W Roy RV Eley R. R., and Petrash S 2001 J. Colloid Interf. Sci., **234** 363

[26] Uchida N 2005 Physica D: Nonlinear Phenomena, **205** 267.

[27] Chua D B Ng H T and Li S F 2009 Appl. Phys. Lett. **76** 721

[28] Remie M J Särner G Cremers M F G Omrane A Schreel K R A M Aldén M de Goey L P H 2008 Int. J. Heat Mass Transfer **51** 1854

[29] Churchill S W and Chu H H S 1975 Int. J. Heat Mass Transfer **18** 1323

[30] Kobus C J and Wedekind G L 2001 Int. J. Heat Mass Transfer **44** 3381

[31] COMSOL AB (2007) Comsol Multiphysics Modelling Guide

[32] Bird R B Stewart W E Lightfoot E N *Transport Phenomena* Wiley New York 1960

[33] Radziemska E and Lewandowski W M 2001 Appl. Energy **68** 347

[34] Geissberger A E and Galeener F L 1983 Phys. Rev. B **28** 3266

[35] McMillan P F Poe B T Gillet Ph and Reynard B 1994 Geochim. Cosmochim. Acta **58** 3653

[36] Galeener F L and Mikkelsen J C Jr. 1981 Phys. Rev. B **23** 5527

[37] Rouhi N Esfandyarpour B Mohajerzadeh S Hashemi P Robertson M D and Raffel K 2010 J. Non-Cryst. Solids **356** 1027

[38] Aguiar H Serra J González P and León B 2009 J. Non-Cryst. Solids **355** 475

[39] Seifert F A Mysen B O and Virgo D 1983 Phys. Chem. Glasses **24** 141

[40] Lucovsky G 1979 Philos. Mag. B **39** 513

[41] Kalampounias A G Yannopoulos S N and Papatheodorou G N 2006 J. Chem. Phys. **124** 014504

[42] Galeener F L and Geissberger A E 1983 Phys. Rev. B **27** 6199

[43] Pasquarello A and Car R 1998 Phys. Rev. B **80** 5145

[44] da Silva S W Pedroza R C Sartoratto P P C Rezende D R da Silva Neto A V Soler M A G and Morais P C 2006 J. Non-Cryst. Solids **352** 1602

[45] Calistru D M Wang W B Petričević V and Alfano R R 1995 Phys. Rev. B **51** 14980

[46] Allen G C Dyke J M Harris S J and Morris A 1988 Oxid. Met. **29** 391

CAPTIONS

Fig. 1: Example of nanostructures grown by chemical vapour deposition enhanced by a remote micro-afterglow at atmospheric pressure. a) nanodots of silica with a mean diameter close to 500 nm get interconnected to create threads. b) 3D nanostructures obtained when the deposition time increases. c) Thicker coatings (~1 µm): SiO_2 walls forming hexagonal cells obtained on a SiO_2 sublayer. d) Even thicker coatings (>1 µm): thin films giving "nestlike structures" made of nanoribbons when put under vacuum.

Fig. 2: Experimental set-up.

Fig. 3: Description of the domain defined for the model and the parameters needed to mesh the stack made by the silica coating and the substrate. h_1, h_2 and h_3 are the heat transfer coefficient at walls 1, 2 and 3. η is the position of surface versus time and radius r. H is the distance between the plasma nozzle and the substrate. L and R are the thickness and the radius of the sample. δ is the diameter of the micro-post-discharge. z is the depth in the sample.

Fig. 4: Time evolution of the temperature radial distribution of the backside surface of the stainless steel substrate with a silica layer under deposition ($y = 21$). Full lines are experimental data and dash lines, data given by the model. a) afterglow temperature is 1200 K and H=6.0 mm. b) afterglow temperature is 1400 K and H=2.8 mm. In one case (dotted lines), the temperature measured when no deposition occurs is also depicted.

Fig. 5: Calculated radial distribution of the temperature of the surface submitted to the afterglow.

Fig. 6: SIMS depth profile of a patterned surface of SiO_2 deposited on a stainless steel substrate. H=3 mm. Treatment time: 10 s. $y = 12$. Plasma mixture: Ar–9.1 vol.% O_2.

Fig. 7: Raman spectra of a stainless steel substrate covered or not by a SiO_2 coating. Treatment time: 10 s. $y = 9$. Plasma mixture: Ar–9.1 vol.% O_2.

Fig. 8: Raman spectra of a stainless steel substrate covered by a SiO_2 coating along the radius. Treatment time: 30 s. $y = 15$. Plasma mixture: Ar–9.1 vol.% O_2.

Fig. 9: Magnification from 620 to 820 cm^{-1} of the Raman spectra depicted in Fig. 7. The spectra are fitted with three main peaks. They are corrected with a linear baseline for better comparison.

Fig. 10: Magnification from 380 to 620 cm^{-1} of the Raman spectra obtained for two treatment: 10 s and $y = 9$ and 10 s and $y = 21$. Plasma mixture: Ar–9.1 vol.% O_2. Spectra are measured at the centre (straight lines) and at the edge (dash line) of the coating. Peaks are fitted with a lorentzian function.

Fig. 11: SIMS radius profiles of the surface of a SiO_2 coating deposited on a stainless steel substrate. The influence of the distance between the nozzle and the substrate is studied. Treatment time: 10 s. $y = 12$. Plasma mixture: Ar–9.1 vol.% O_2.

Table 1: Gas properties used in the model of heat transfer.

Table 2: Solid properties used in the model of heat transfer.

Gas	Properties	Temperature range	Fitting functions
Ar	Cp (J/kg/K)	[100-2000 K]	$519.65 + 6.73909 \times 10^{-6}\ T - 3.66027 \times 10^{-6}\ T^2 + 2.73033 \times 10^{-7}\ T$
	λ (W/m/K)		$3.04979 \times 10^{-4} + 6.62052 \times 10^{-5}\ T - 2.99436 \times 10^{-8}\ T^2 + 6.79149 \times 10^{-12}\ T^3$
	μ (kg/m/s)		$5.29435 \times 10^{-7} + 8.39206 \times 10^{-8}\ T - 3.73959 \times 10^{-11}\ T^2 + 8.45217 \times 10^{-15}\ T^3$
	ρ (kg/m^3)		$487.432 \times T^{-1}$
O$_2$	Cp (J/kg/K)	[100-2000 K]	$872.77846 + 6.719 \times 10^{-2}\ T + 4.34497 \times 10^{-4}\ T^2 - 3.83385 \times 10^{-7}\ T^3 + 8.86794 \times 10^{-11}\ T^4$
	λ (W/m/K)		$0.00249 + 8.9486 \times 10^{-5}\ T - 2.32256 \times 10^{-8}\ T^2 + 4.13867 \times 10^{-12}\ T^3$
	μ (kg/m/s)		$3.3958 \times 10^{-6} + 5.87982 \times 10^{-8}\ T - 2.13186 \times 10^{-11}\ T^2 + 4.41967 \times 10^{-15}\ T^3$
	ρ (kg/m^3)		$389.946 \times T^{-1}$
Dry air	Cp (J/kg/K)	[175-1900 K]	$1032.10308 - 0.29542\ T + 8.27169 \times 10^{-4}\ T^2 - 5.35621 \times 10^{-7}\ T^3 + 1.12295 \times 10^{-10}\ T^4$
	λ (W/m/K)		$7.50556 \times 10^{-4} + 9.42622 \times 10^{-5}\ T - 3.38667 \times 10^{-8}\ T^2 + 6.56677 \times 10^{-12}\ T^3$
	μ (kg/m/s)		$2.80339 \times 10^{-6} + 5.87333 \times 10^{-8}\ T - 2.52496 \times 10^{-11}\ T^2 + 5.41836 \times 10^{-15}\ T^3$
	ρ (kg/m^3)		$353.05395 \times T^{-1.00002}$
	β		$0.99471 \times T^{-1} + 3.02658 \times 10^{-5} - 5.47422 \times 10^{-8}\ T + 3.34974 \times 10^{-11}\ T^2 - 7.68954 \times 10^{-15}\ T^3$

Table 1 (Table1.jpg)

Solid	Properties	Temperature range	Fitting functions
Silica	λ (W/m/K)	[10-2000 K]	$1.96947 - \{261951.7998$ $/ (1+\exp((T + 3178.46501) / 268.83446)\}$
	Cp (J/kg/K)	[298-2000]	$931.7229 + 2.56258 \times 10^{-1} T$ $- 2.402425 \times 10^{7} / T^{2}$
	ρ (kg/m^3)		8940
Stainless Steel	λ (W/m/K)	[200-2000 K]	$9.0109 + 1.5298 \times 10^{-2} T$
	Cp (J/kg/K)	[298-1358 K]	$365.43 + 0.40649 \times T - 1.7321 \times 10^{-4} T^{2}$
	ρ (kg/m^3)		7900

Table 2 (Table2.jpg)
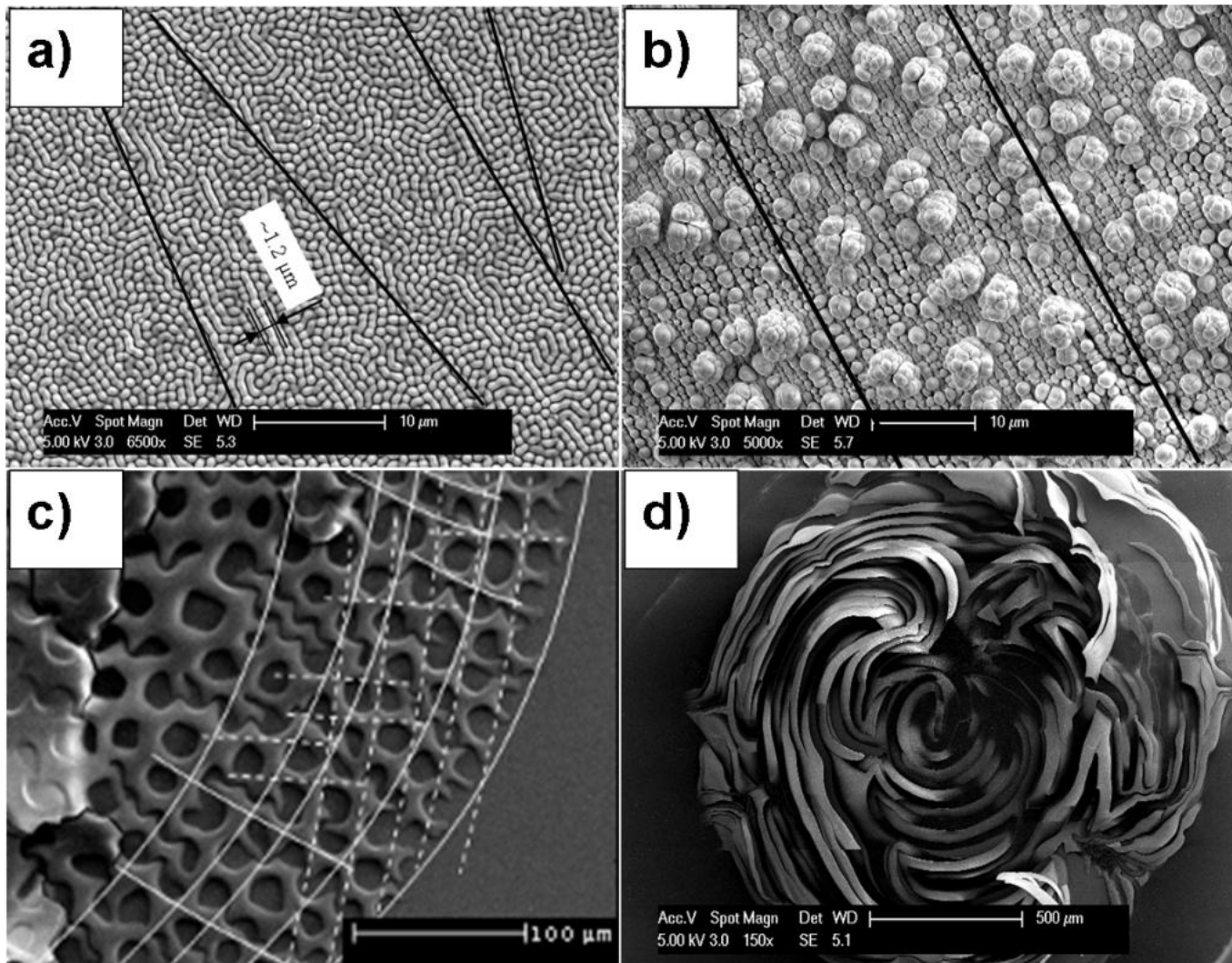
Figure 1 (Figure1.jpg)
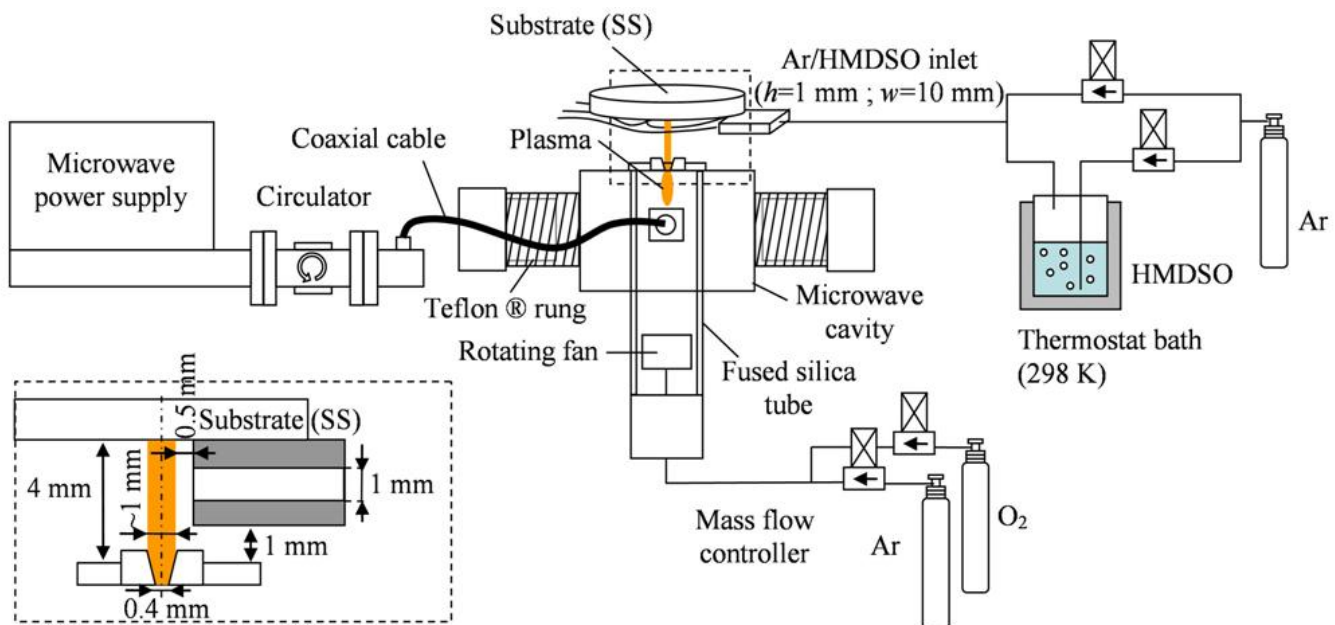
Figure 2 (Figure2.jpg)
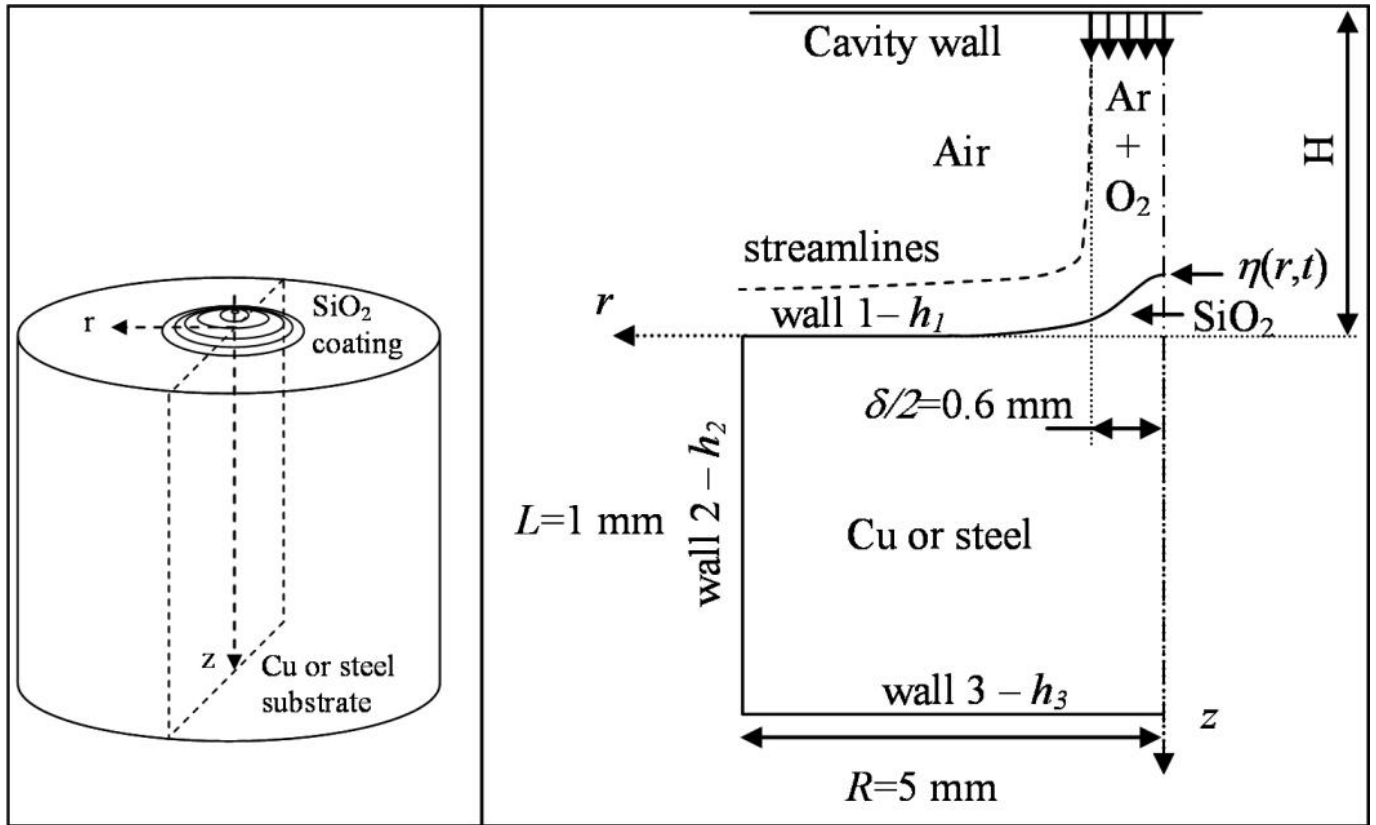
Figure 3 (Figure3.jpg)
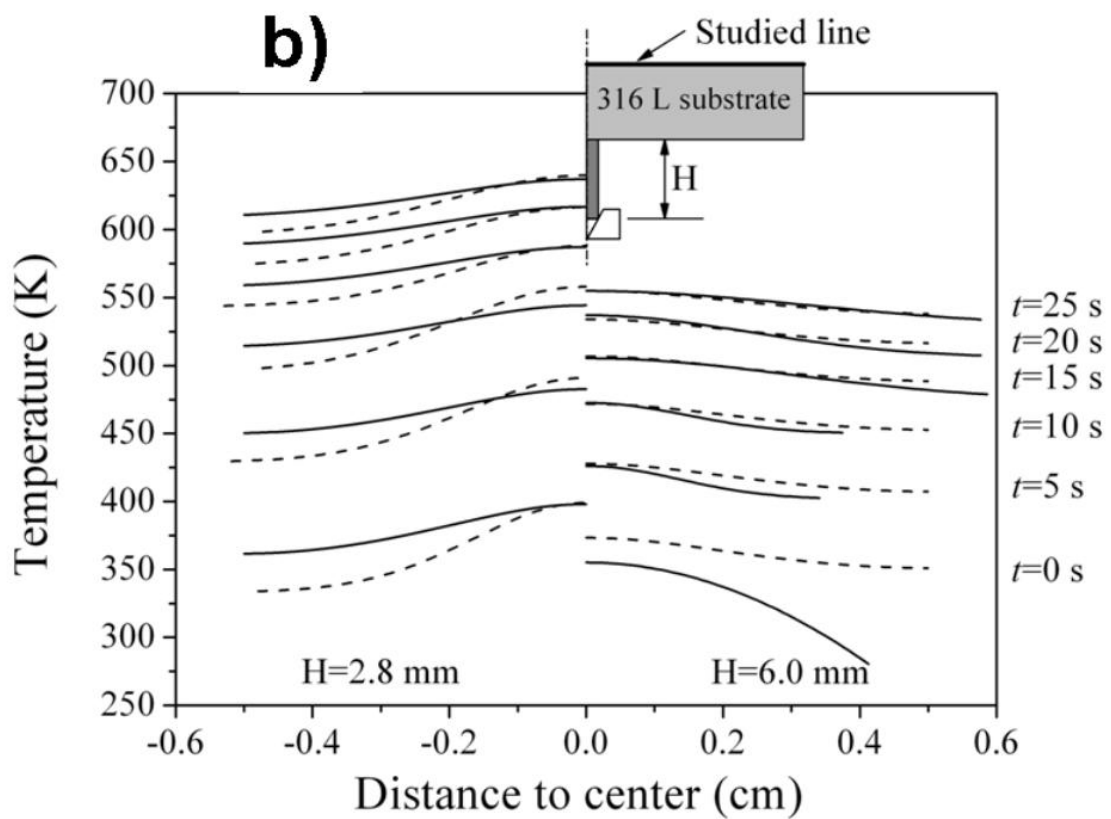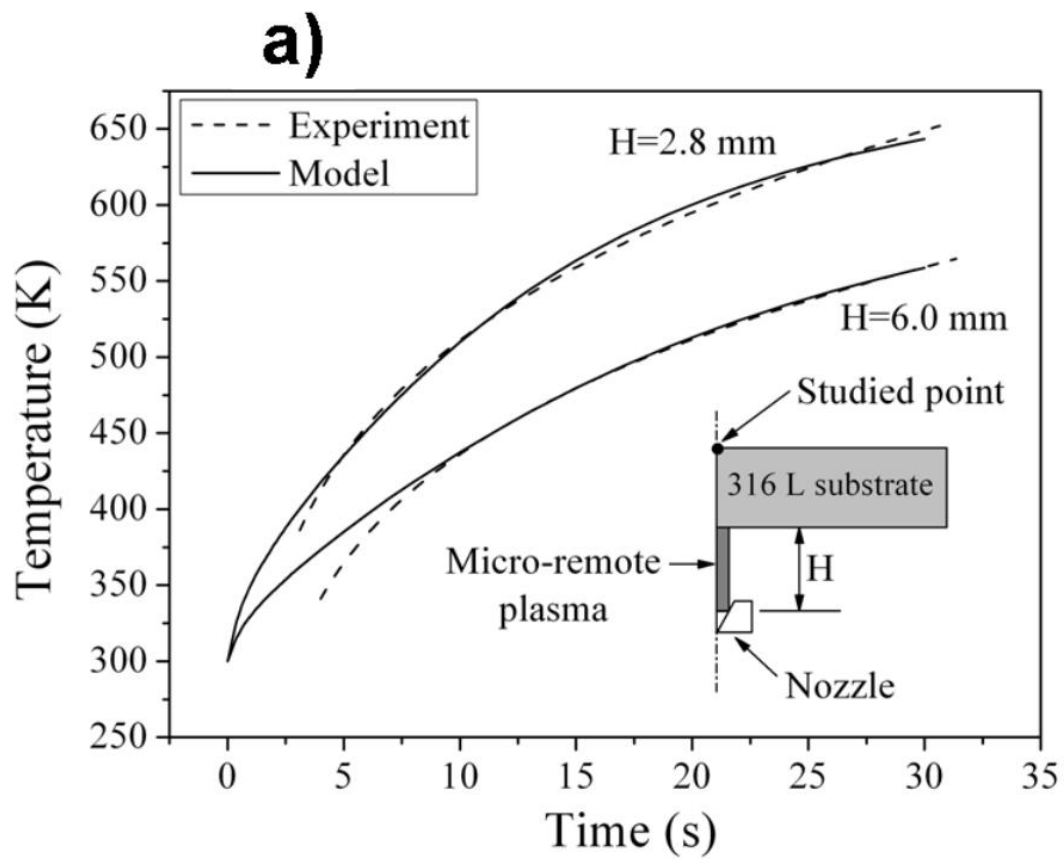
Figure 4 (Figure4.jpg)
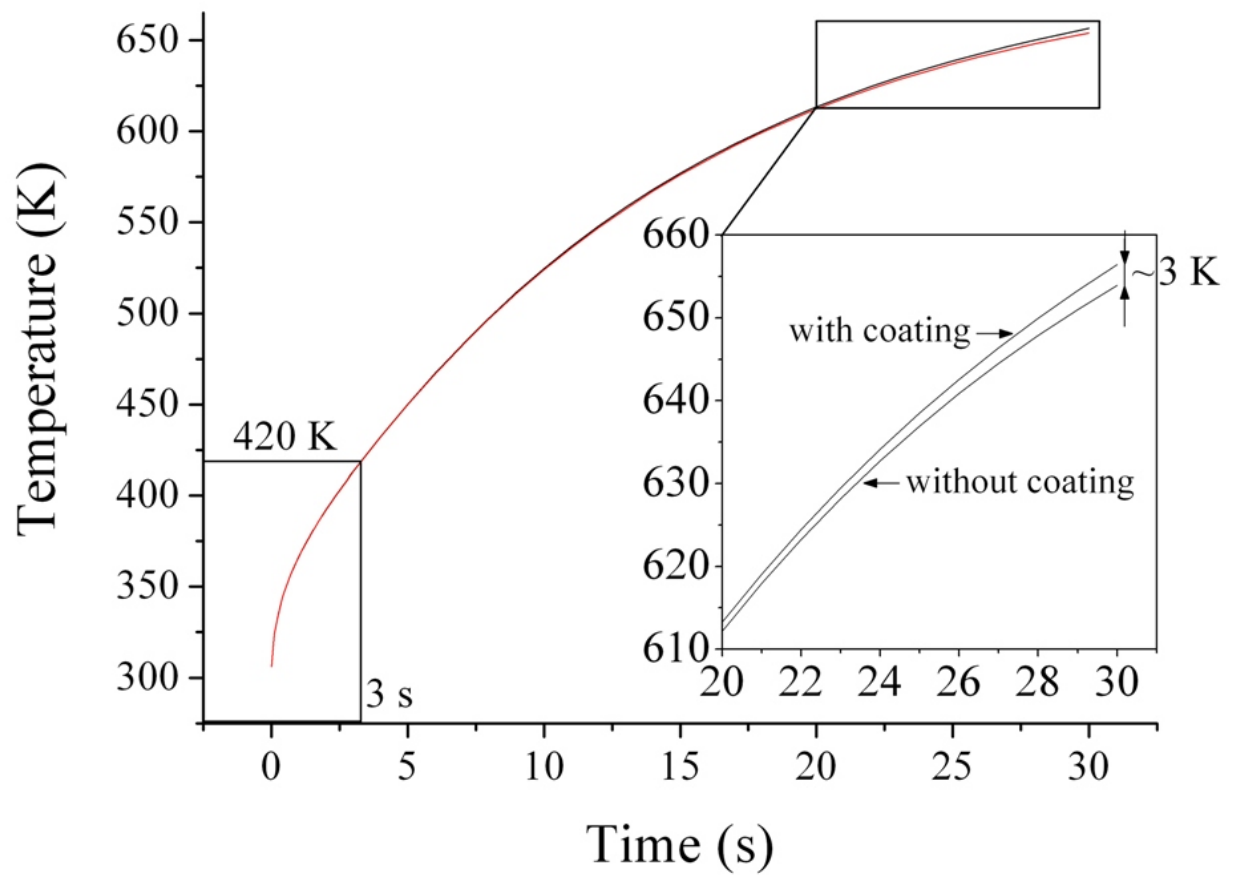
Figure 5 (Figure5.jpg)
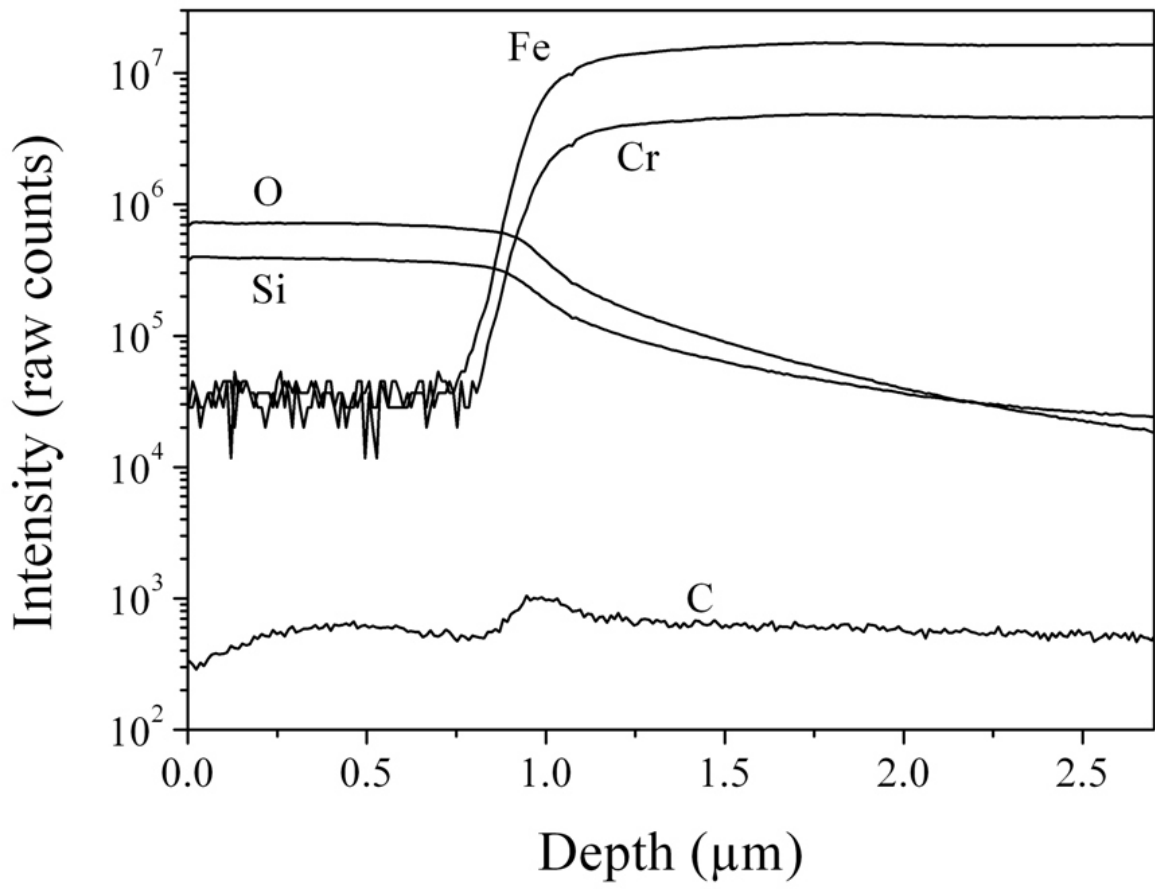
Figure 6 (Figure6.jpg)
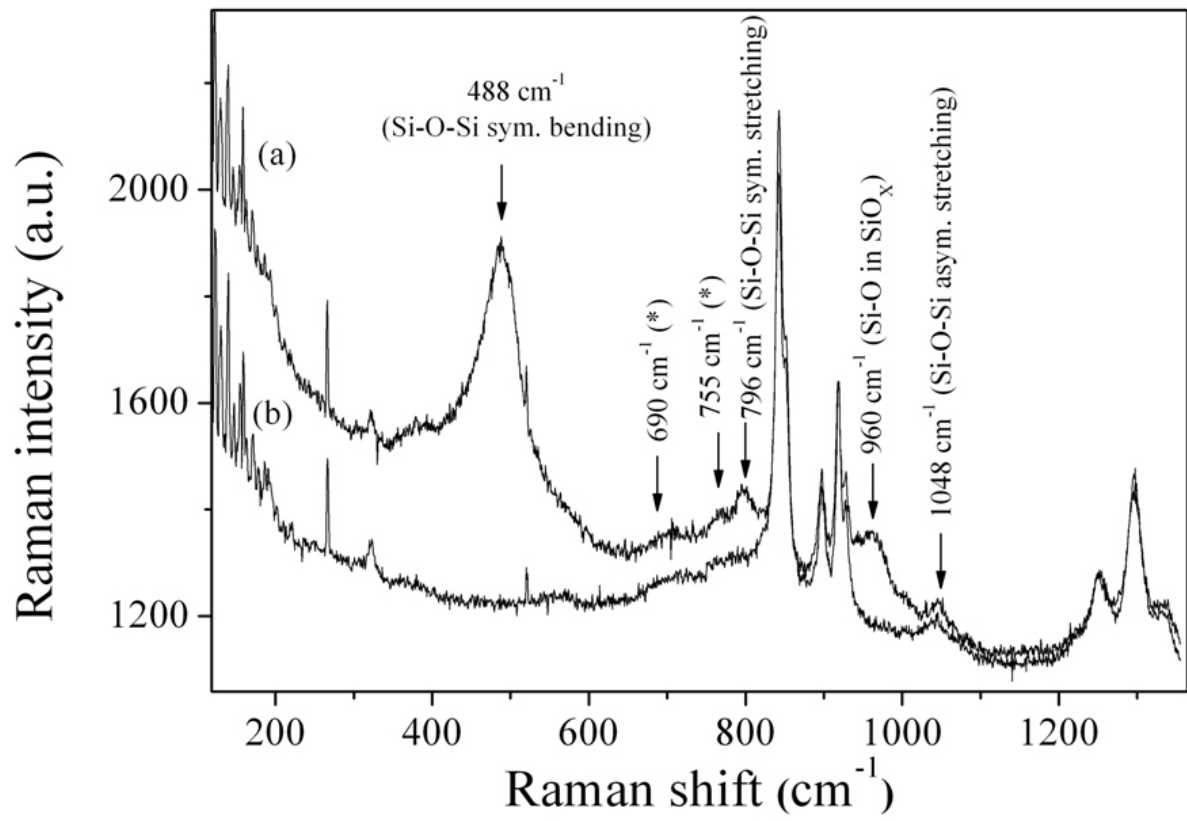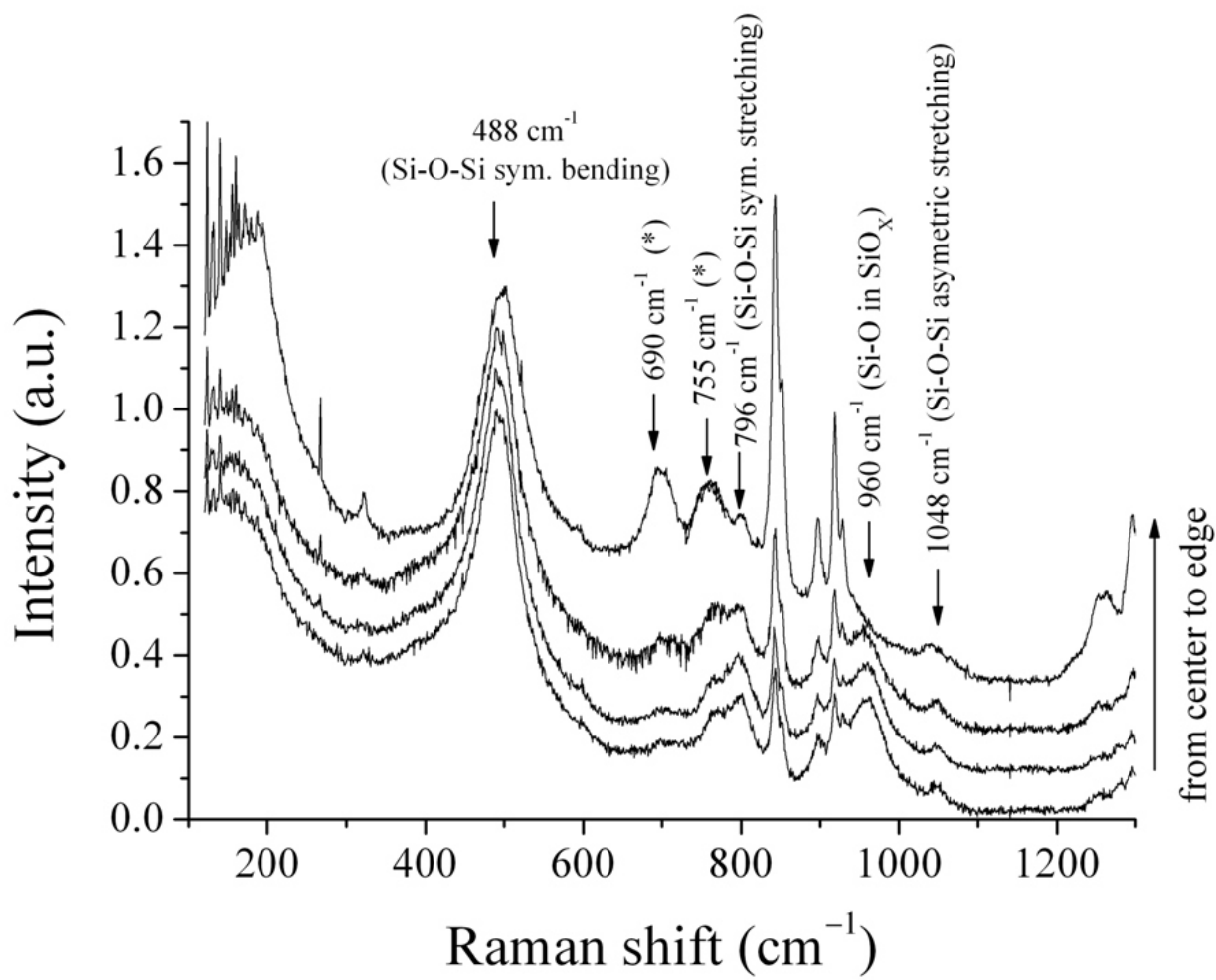
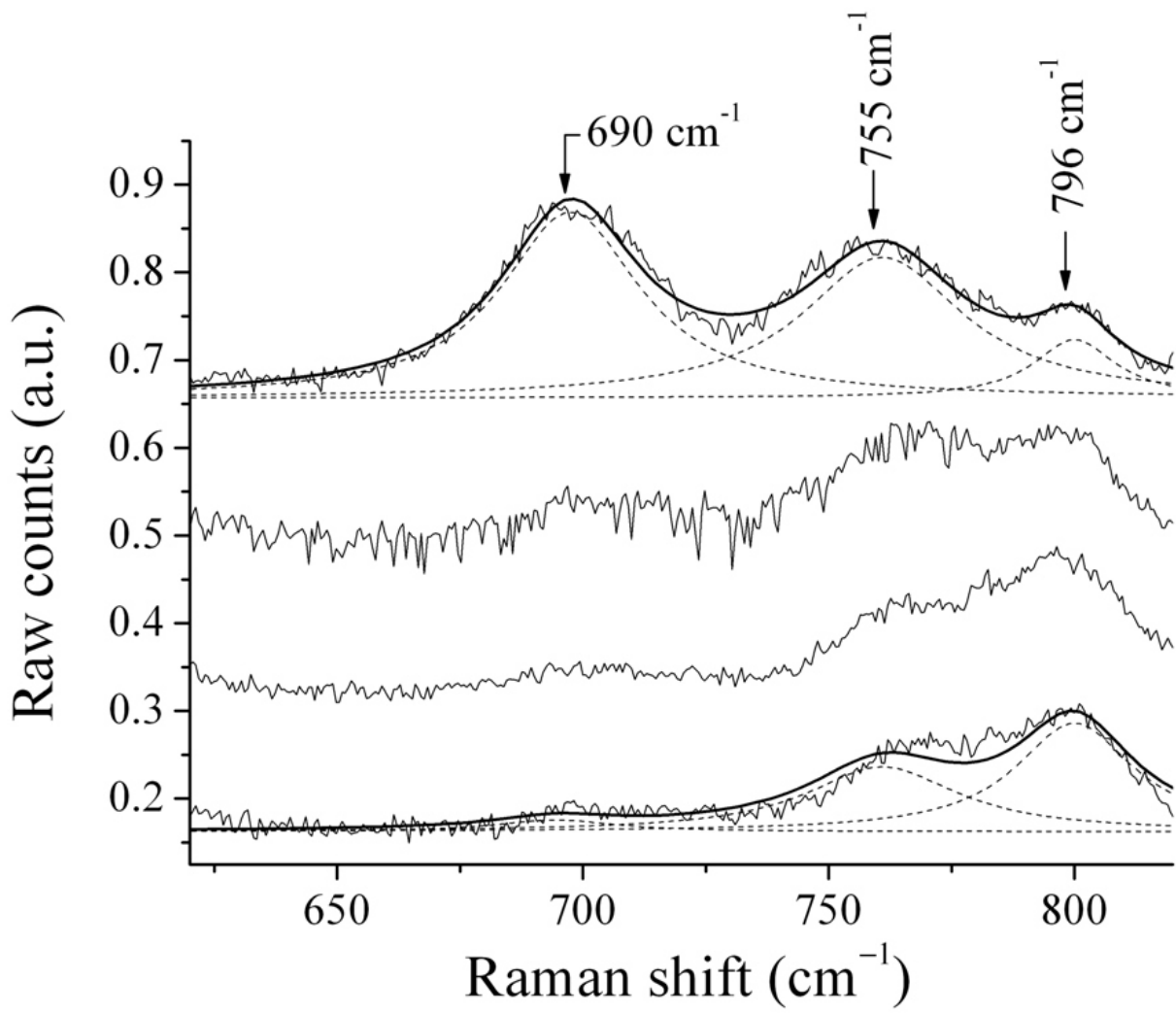**Figure 7 (Figure7.jpg)**
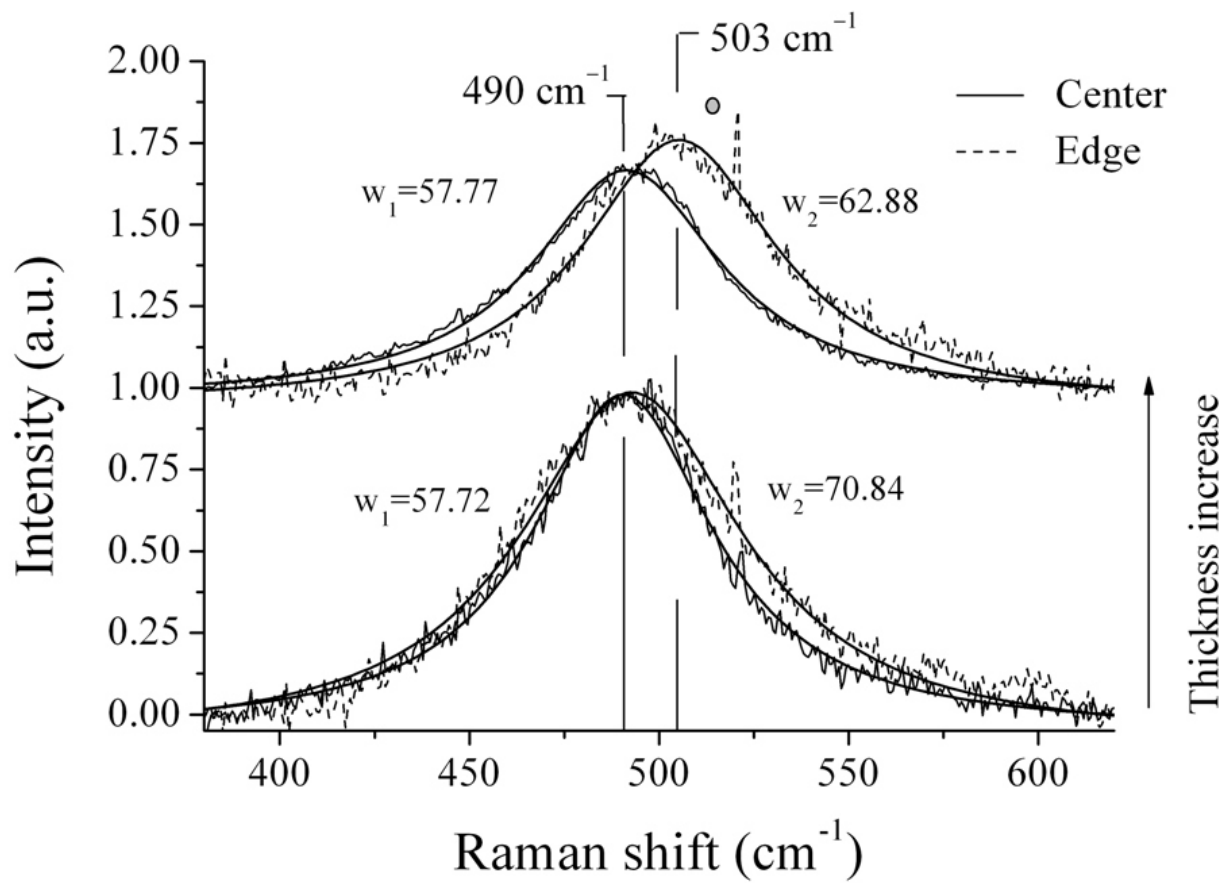
Figure 8 (Figure8.jpg)

Figure 9 (Figure9.jpg)
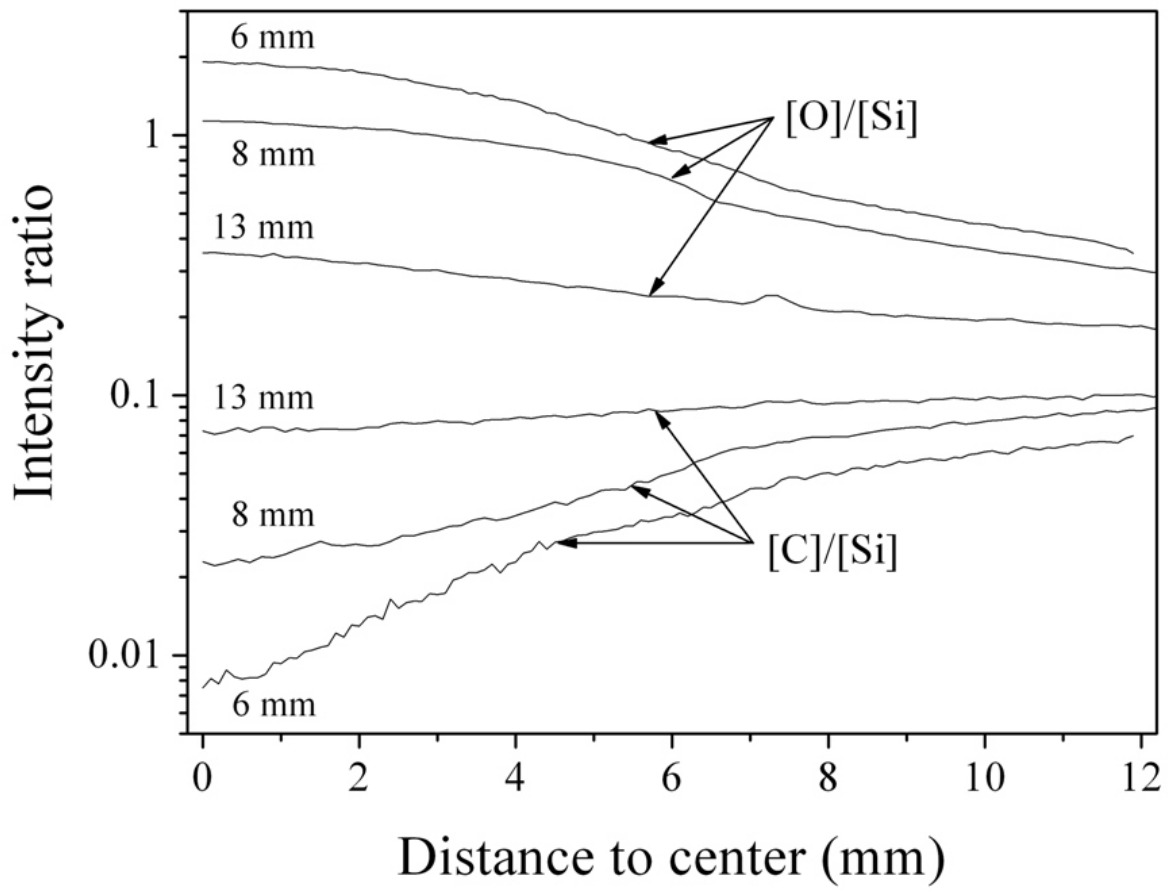
Figure 10 (Figure10.jpg)

Figure 11 (Figure11.jpg)